PAPER

Check for updates

Investigating the asymmetric electrochemical, structural and electronic properties of Mn-rich Li(Mn,Fe)PO$_4$ electrode materials

Beatrice Ricci, [ID] *[abc] Felix-Cosmin Mocanu, [ID] [a] Dimitrios Chatzogiannakis, [ID] [bd] Victor Fuentes, [bd] Ashley P. Black, [ID] [bd] Benoît Cluzeau, [ID] [e] Cécile Tessier, [e] Patrick Bernard, [e] M. Saiful Islam [ID] *[ac] and M. Rosa Palacín [ID] *[bc]

Olivine-type phosphates LiMn$_x$Fe$_{1-x}$PO$_4$ are attracting increasing interest as positive electrode materials for lithium-ion batteries due to their low cost and good electrochemical performance. However, the effects of the mixed Mn/Fe composition on lithium intercalation and ion transport are not fully characterised, especially in Mn-rich compositions. In this study, the electrochemical, structural and ion transport properties of Mn-rich LiMn$_x$Fe$_{1-x}$PO$_4$ ($x = 0.6, 0.7, 0.8$) (LMFP) are investigated using a combination of experimental and materials modelling techniques. Considerable asymmetry in charge/discharge profiles is found, which highlights the complexity of the mixed-metal system. An intricate lithium intercalation mechanism is observed, including both solid solution and two-phase regions. While the Fe/Mn cation disorder causes the oxidation to proceed mostly *via* a solid solution mechanism, the Mn plateau remains associated with a two-phase process. *Ab initio* simulations indicate that Li$^+$ diffusion occurs along one-dimensional channels parallel to the crystallographic *b*-axis following a curved trajectory, and find favourable Li/Fe and Li/Mn anti-site defect formation. Analysing the band gaps of the lithiated and delithiated phases revealed that Mn substitution of Fe can improve the electronic conductivity, suggesting asymmetric electronic behaviour.

1. Introduction

Rechargeable lithium-ion batteries (LIBs) are currently the leading electrochemical energy storage technology, with applications ranging from portable electronics to electric vehicles and grid-scale energy storage. The olivine phosphate LiFePO$_4$ (LFP) gained popularity as a positive electrode material in LIBs after early pioneering work by Padhi *et al.*;[1] and is growing in commercial relevance due to its low cost, excellent stability and good electrochemical performance.[2–15] However, this compound suffers from low gravimetric energy density, voltage, and electronic conductivity. Studies have attempted to compensate these issues through Fe substitution by other electrochemically-active ions, with solid solutions of Mn and Fe in LiMn$_x$Fe$_{1-x}$PO$_4$ (LMFP) allowing access to the Mn^{2+}/Mn^{3+} redox couple (4.1 V *vs.* Li$^+$/Li compared to 3.45 V for Fe^{2+}/Fe^{3+}), considerably raising the operating voltage compared to its pure Fe counterpart.[4,16–19] This has triggered growing interest in Mn-rich LMFP as promising high voltage cathodes.[18,20–28] Mn-rich compositions were considered commercially unviable due to the intrinsic instability caused by Jahn–Teller distortions around Mn^{3+}.[29] The benefits of Mn-rich compositions' higher operating voltage therefore remain difficult to evaluate as the lithium intercalation, ion transport and defect formation mechanisms are not fully characterised.[11,30–37] Additionally, Mn redox activity is associated with slower kinetics, which then leads to higher electrode polarisation and cell overpotentials.

Due to these issues, previous studies have largely focused on the Fe-rich compositions using a diverse range of electrode manufacturing techniques;[16,30,38] this has led to conflicting conclusions in a system where electrochemistry strongly depends on electrode preparation methods, which can significantly influence ionic and electronic conductivity. In this study, the electrochemical, structural and ion transport properties of commercial Mn-rich LiMn$_x$Fe$_{1-x}$PO$_4$ ($x = 0.6, 0.7, 0.8$) are investigated using a range of experimental and materials modelling methods including potentiostatic intermittent titration technique (PITT), *operando* X-ray diffraction (XRD), *operando* X-ray absorption near edge spectroscopy (XANES) and density functional theory (DFT). The experimental part of this investigation follows adapted industrial electrode manufacturing processes to consistently prepare high-loading LMFP electrodes.

[a]Department of Materials, University of Oxford, Parks Road, Oxford OX1 3PH, UK. E-mail: beatrice.ricci@materials.ox.ac.uk; saiful.islam@materials.ox.ac.uk

[b]ICMAB-CSIC, Campus UAB, 08193 Bellaterra, Spain. E-mail: rosa.palacin@icmab.es

[c]ALISTORE European Research Institute, FR CNRS 3104, 80039 Amiens Cedex, France

[d]CELLS-ALBA Synchrotron, 08290 Cerdanyola del Vallès, Barcelona, Spain

[e]Saft Bordeaux, 111, Bd. Alfred Daney, 33300 Nouvelle-Aquitaine, France

The study reveals considerable asymmetry between charge and discharge in terms of electrochemical behaviour, electronic properties, and (de)lithiation mechanism in the Mn-rich system. Electrochemical testing reveals greater kinetic limitations on charge, with important implications for charging protocols in commercial applications. The lithium intercalation mechanism includes solid solution and two-phase regions; while the Fe/Mn cation disorder causes the oxidation to proceed mostly *via* a solid solution mechanism, the Mn plateau remains associated with a two-phase process. Analysing the band gaps of the lithiated and delithiated phases through *ab initio* simulations shows that Mn substitution of Fe can improve electronic conductivity.

2. Results and discussion

2.1 Electrochemical performance

Fig. 1 shows representative oxidation and reduction curves for the electrodes in coin cells against lithium metal counter electrodes at two different rates (C/10 and 3C). All three compositions (LiMn$_x$Fe$_{1-x}$PO$_4$, x = 0.6, 0.7 and 0.8) demonstrate two voltage plateaus, typical of two-phase reactions, connected by a sloping region. Considerable differences in voltage curve shape can be seen in Fig. 1 depending on the Fe/Mn ratio, with the higher voltage plateau lengthening and the lower voltage plateau contracting as Mn concentration increases. The plateau above 4 V can therefore be tentatively assigned to the Mn^{3+}/Mn^{2+} couple and the plateau around 3.5 V to the Fe^{3+}/Fe^{2+} couple. Higher average discharge voltages are therefore obtained with higher Mn content (3.75, 3.82, and 3.88 V for x = 0.6, 0.7, and 0.8 at C/10, respectively). All three compositions give similar discharge capacities at a rate of C/10 (146, 141 and 145 mAh g^{-1} for x = 0.6, 0.7, and 0.8, respectively, see Fig. S1), consistent with the values ranging from 125 to 155 mAh g^{-1}
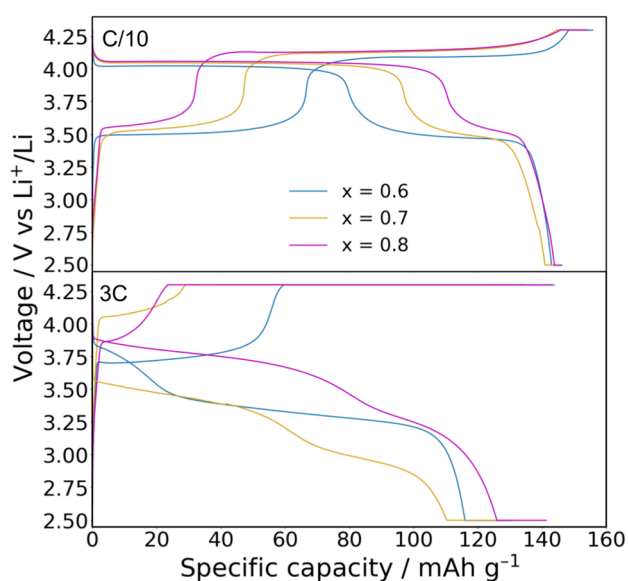
obtained in previous studies with $x \geq 0.5$.[6,7,18–21,23,26–28,39,40] Generally, higher voltages are observed for the same plateaus as Mn concentration increases: this may be due to poor kinetics, leading to increased overpotentials, or thermodynamic factors such as the inductive effect.

At a higher rate (3C), the curves differ significantly. Fig. 1b shows sloping profiles for both charge and discharge for all compositions with high polarisation, suggesting the existence of a single phase region where both Mn and Fe are redox-active and form a solid solution.[18,20,40] This is emphasised on charge for the higher Mn concentrations, suggesting greater kinetic limitations on charge. Interestingly, the length of the plateaus and the degree of polarisation differ substantially between charge and discharge, especially at high rate. Polarisation is much higher during charge than during discharge, with most of the capacity only being recovered during the constant voltage step. This may be due to differences in electronic structure between the lithiated and delithiated phase, with kinetics on charge potentially limiting the accessible capacity that can be recovered without a voltage hold. The testing protocol employed was selected so as to exclude the influence of additional factors such as electrolyte oxidation at high voltages. This has been shown to be negligible in electrolyte systems such as the system used below 4.3 V *vs.* Li$^+$/Li,[41,42] with significant electrolyte degradation only occurring above 4.5 V.[43,44]

Notable differences in discharge capacity are also visible: 114, 110, and 124 mAh g^{-1} were reached for x = 0.6, 0.7, and 0.8, respectively, indicating good rate capability. The capacities reached are equivalent to 78.0, 78.0 and 85.3% of the values obtained at C/10. Fig. S1 shows that the x = 0.6 and 0.7 compositions reach similar capacities (within 1 standard deviation of each other), while the x = 0.8 system reaches significantly higher capacities. Higher Mn content does not appear to hinder rate capability but rather enhances it in some cases. Fig. S2 shows the dQ/dV plots generated from this cycling data; a clear increase in overpotential is seen for all three compositions at higher rates, suggesting kinetic limitations are especially important for rates of 1C and above. Again, the oxidation and reduction branches differ in peak intensity, indicating asymmetric behaviour consistent with the polarisation differences observed in Fig. 1.

PITT measurements give thermodynamic information and provide precise values for reaction voltage and overpotentials (the difference between oxidation and reduction peaks) at near-equilibrium conditions. Fig. 2 shows the incremental capacity (IC) plots obtained from PITT measurements, from which complementary thermodynamic data can be extracted. The IC voltammograms for individual electrodes and their charge–discharge profiles, as well as the stepped voltage profiles and current responses from the PITT measurements, can be found in the SI (Fig. S3 and S4).

As reported previously,[29,34,38,45] higher Mn content increases both the intensity of and the area under the peak related to the Mn plateau, as well as the voltage of the Fe^{2+}/Fe^{3+} couple (3.49, 3.51 and 3.54 V *vs.* Li$^+$/Li for x = 0.6, 0.7, and 0.8, respectively). This is attributed to a stronger inductive effect for the softer Mn^{2+} cation (radius = 0.83 Å) than for the Fe^{2+} cation (0.78 Å)[46]
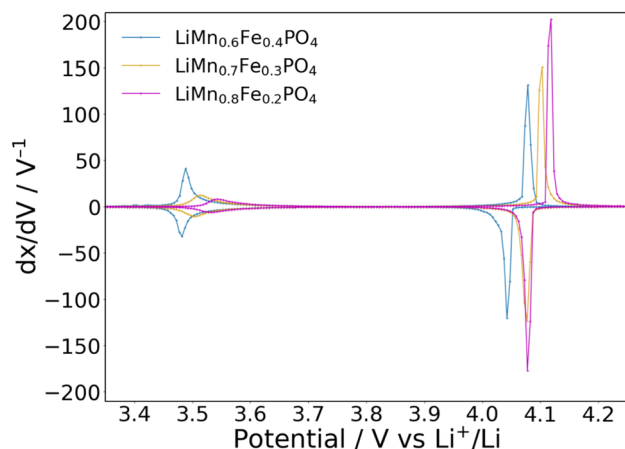

Fig. 1 Cycling profiles of LiMn$_x$Fe$_{1-x}$PO$_4$ (x = 0.6 in blue, 0.7 in yellow, 0.8 in magenta), measured in CR2032 coin cells *vs.* lithium at a C-rate of C/10 (top) and 3C (bottom) with a 0.5 hour voltage hold at cutoffs.

Fig. 2 IC voltammograms of $LiMn_xFe_{1-x}PO_4$ ($x = 0.6$ in blue, 0.7 in yellow, 0.8 in magenta), as obtained from PITT with 5 mV potential steps and a limiting current equivalent to a C/100 cycling rate.

and the Fe–O–Mn superexchange interaction increasing the voltage of the Fe couple. A clear increase in voltage for the Mn^{2+}/Mn^{3+} couple is also seen with increasing Mn concentration (4.06, 4.09 and 4.10 V $vs.$ Li^+/Li), in accordance with the work of Di Lecce et $al.$,[38] and in contrast with the negligible changes reported by Zhang et $al.$[34] and Niu et $al.$[45]

The plateau overpotentials show minor variations with the Fe/Mn ratio, remaining at around 10 mV for the Fe reaction and 30 mV for the Mn reaction. This suggests that the increase in plateau voltage with increasing Mn concentration observed in Fig. 1 is not due to thermodynamic factors but due to sluggish electrode kinetics, as suggested by the dQ/dV comparison shown in Fig. S2. These ΔV values are slightly lower than previously observed.[27,28,34,38,45] Fig. 3 shows the evolution of voltage profiles upon cycling the electrodes for up to 100 cycles
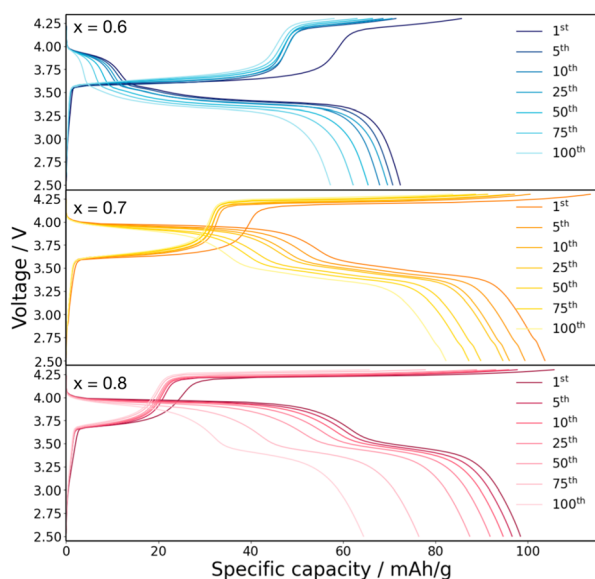

Fig. 3 1st, 5th, 10th, 25th, 50th, 75th, and 100th charge and discharge voltage profiles for $x = 0.6$ (top), $x = 0.7$ (middle), and $x = 0.8$ (bottom) measured in 2032-type coin cells $vs.$ lithium at a rate of 1C.

at 1C. Over time, both voltage and capacity decay, with greater percentage losses observed for $x = 0.8$. Similar final capacities were obtained for all three materials tested.

2.2 $Operando$ X-ray diffraction and absorption near edge spectra

To monitor the structural and electronic changes during a full charge–discharge cycle at C/10, synchrotron $operando$ X-ray diffraction (XRD) and X-ray absorption near-edge spectra (XANES, Fe and Mn K-edges) were collected (see SI Fig. S5 and S6). XRD provides long-range structural information, while XANES spectra provide complementary information on the oxidation states present in the material. Fig. 4 shows the evolution of a selected region of the diffraction pattern for $LiMn_xFe_{1-x}PO_4$ ($x = 0.7$) for a full cycle (charge and discharge) at C/10; patterns for the other materials are similar and available in the SI (Fig. S5). Fig. S6 shows the variation in X-ray absorption intensity at 6553 eV and 7128 eV, which correspond to the maximum of the Mn^{3+} and Fe^{3+} white lines respectively, with the cell voltage. The combined diffraction and absorption datasets confirm that the two plateau regions observed electrochemically originate from distinct and non-overlapping redox processes. The lower voltage plateau is exclusively associated with the Fe^{2+} to Fe^{3+} oxidation, while the higher voltage plateau corresponds solely to the Mn^{2+} to Mn^{3+} redox reaction. No region of simultaneous Fe and Mn activity is detected for any of the three compositions. Furthermore, increasing the Mn content systematically enlarges the voltage span of the Mn plateau, consistent with the extended presence of the Mn redox signature at 6553 eV.

The Rietveld-derived phase fractions demonstrate that the extent of the solid solution regime decreases progressively with increasing Mn content. Mn substitution suppresses the miscibility gap that drives the strictly two-phase $Li(Mn,Fe)PO_4$ to $(Mn,Fe)PO_4$ transition, thereby stabilising intermediate compositions and allowing a wider continuous solid solution pathway. Interestingly, the solid solution regime extends beyond the Fe plateau into the early portion of Mn oxidation, which may indicate the LMFP structure tolerating a limited amount of Mn^{2+} to Mn^{3+} conversion before the phase transition starts. The extent of this overlap is inversely proportional to Mn concentration: Mn-rich compositions tolerate only a small degree of Mn oxidation before nucleation of the MFP phase starts, whereas Fe-rich compositions show a significantly broader overlap. As a result, full conversion to the MFP end member at the end of charge is achieved only for the Mn-rich composition ($x = 0.8$), whereas the more Fe-rich samples retain around 30% LMFP phase. The $operando$ cells reach similar capacity values (144, 152, and 147 mAh g^{-1} for $x = 0.6$, 0.7, 0.8 respectively) to those of the previous electrochemical tests at C/10, so this is not caused by incomplete oxidation. Fig. 5 summarises the range of lithiation states across which solid solution and two-phase behaviour are observed for the compositions tested. Unit cell volumes and phase fractions obtained from the sequential Rietveld refinement of $operando$ synchrotron XRD and are depicted in Fig. 6, S7 and S8.
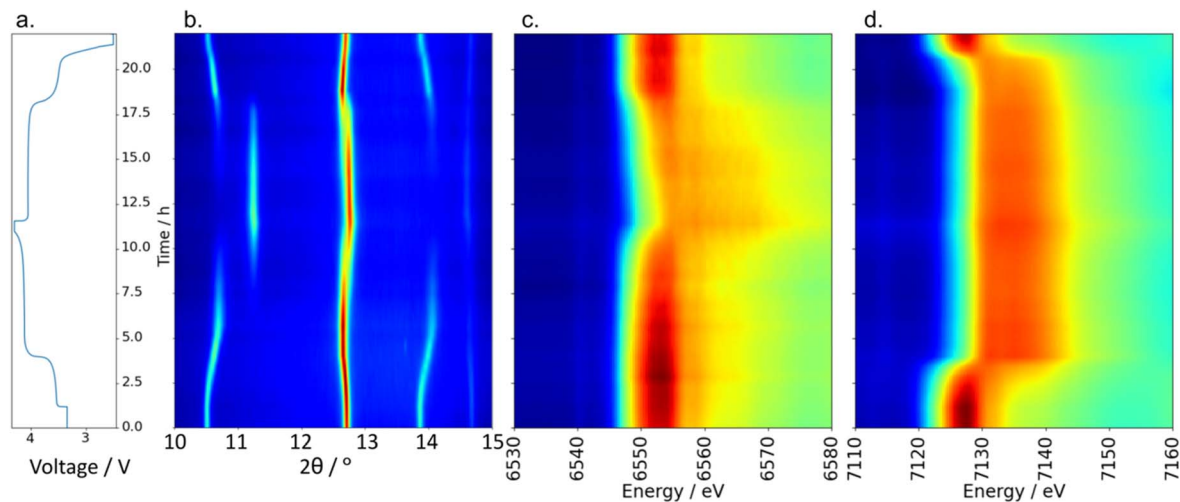
Fig. 4 Data for the $x = 0.7$ composition showing the (a) voltage profile, (b) diffraction pattern in the $2\theta = 10-15°$ region, (c) Mn and (d) Fe K-edges for one full cycle at C/10 recorded at 13 keV ($\lambda = 0.952729$ Å).

A solid solution mechanism is observed during the lower-voltage plateau. This result is in contrast with the two-phase behaviour observed in LFP and LMP.[1] The (200) reflection is initially observed around $2\theta = 10.5°$ but shifts gradually to higher angles as lithium is extracted, reflecting a contraction in interplanar spacing and overall unit cell volume. Similarly, the (020) peak is initially around $2\theta = 18.1°$ and shifts gradually to $18.7°$ towards the end of Fe plateau. XANES spectra show a simultaneous shift in the Fe K-edge from 7125 to 7130 eV, corresponding to Fe^{2+} oxidation to Fe^{3+}, while the Mn K-edge remains unchanged, confirming that Fe is the dominant redox-active species in this region.

Fig. 6 presents the evolution of the LMFP and MFP phase fractions and the corresponding cell volumes obtained by Rietveld refinement of the *operando* XRD data for $x = 0.6$, 0.7,

and 0.8. The largest volume changes occur within the LMFP solid solution region, as expected for continuous lithium extraction. However, residual volume variations persist throughout the two-phase region, which seems to indicate that a minor solid solution contribution remains during both charge and discharge. Generally, higher Mn concentration leads to higher MFP phase fractions in the two-phase region, with the $x = 0.8$ composition including a small window of solid solution MFP compositions at low lithiation, as well as lower variations in unit cell volume, potentially due to the full conversion of LMFP to MFP at the top of charge.

Partial substitution of Fe by Mn introduces cation disorder and lattice flexibility, thermodynamically stabilising intermediate Li compositions and reducing the miscibility gap that drives phase separation in LFP and LMP. This results in a solid
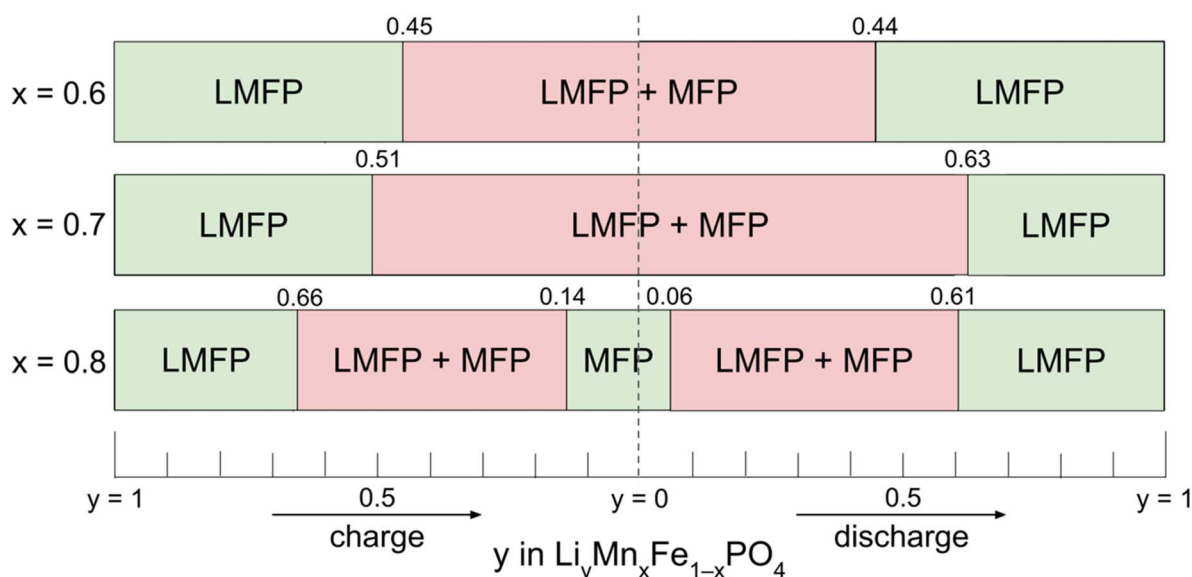

Fig. 5 Regions of solid solution (green, LMFP or MFP only) and two-phase (red, LMFP + MFP) compositions for the LMFP compositions tested, derived from Rietveld refinement (shown in Fig. 6 and S7) of the consecutive *operando* XRD patterns.
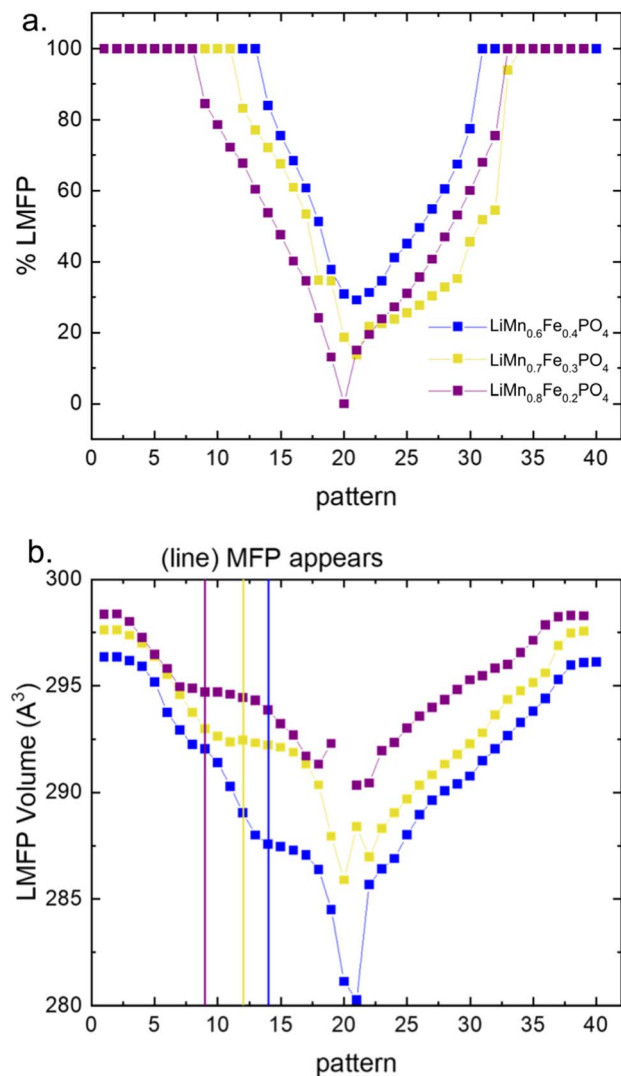
Fig. 6 Comparative representation of LiMn$_x$Fe$_{1-x}$PO$_4$ phase fractions (a) and cell volumes (b) obtained from sequential Rietveld refinements of *operando* X-ray diffraction pattern for $x = 0.6$, 0.7, and 0.8. Vertical lines in (b) mark the appearance of the delithiated MFP phases.

solution mechanism over the Fe redox region, even while Mn is not yet electrochemically active. A solid solution mechanism favours lithium diffusion, as ions do not have to diffuse across interfaces with mismatched lattice parameters. The lithium intercalation mechanism remains two-phase when Mn becomes active at the higher voltage plateau, producing lattice strain and leading to broader diffraction peaks. This coincides with findings for lower Mn concentrations by Yamada *et al.*[29] and Zhang *et al.*[34] As the Mn fraction increases, the Fe plateau and its associated solid solution region contract, shifting towards Mn-dominated two-phase behaviour.

A clear asymmetry between charge and discharge also emerges in both XRD and XAS datasets, with the evolution of the LMFP phase fraction and the Mn^{3+} absorption intensity at 6553 eV exhibiting different slopes during lithiation and delithiation. This is present for all compositions and is attributed to the formation of Jahn–Teller distorted Mn^{3+} during the high-

voltage plateau. The accompanying local strain fields and changes in Li$^+$ diffusion kinetics modify the overall reaction pathway, producing a measurable hysteresis between charge and discharge. The asymmetry is more pronounced for higher Mn concentrations, as seen in Fig. 5 and 6a, with the solid solution being shorter on discharge than on charge. This asymmetry is unlikely to be caused by factors such as interfacial impedance, since it mirrors the electrochemical asymmetry observed in Section 2.1 which was reproduced over multiple, successive cycles, rather than evolving over time. Electrode manufacturing and architecture are also unlikely to be the cause of this structural asymmetry, as this should influence the electrolyte penetration and ion conduction properties equally on charge and discharge.[47]

2.3 Atomistic insights into defects and ion migration

In synergy with our experimental work, *ab initio* materials modelling studies were carried out to gain atomic-scale insights into defect processes, ion migration mechanisms and band gap changes. The crystal structures of the end members LiFePO$_4$ and LiMnPO$_4$ were simulated first, followed by the Mn-rich materials LiMn$_x$Fe$_{1-x}$PO$_4$ ($x = 0.6$, 0.7, 0.8). These are olivine-type structures with the *Pnma* space group, containing PO$_4$ tetrahedra with transition metal ions on edge-sharing octahedral positions with linear channels for Li$^+$ diffusion parallel to the *b*-axis. Table 1 compares the calculated structural parameters from our DFT simulations and experimental values. The calculated unit cell parameters accord well with experiment, deviating by at most 1.5%, indicating that our modelling approach can be used reliably in defect and ion migration calculations of the Mn-rich LMFP materials. This work extends our previous simulation studies on related cathode materials including LiMPO$_4$ (M = transition metal)[48–50] and Mn-rich oxides.[51]

LMP has larger lattice parameters than LFP, consistent with a larger unit cell accommodating the larger Mn^{2+} ion. As Mn concentration increases, the unit cell parameters increase linearly to accommodate the larger metal ion, adhering to Vegard's law (see SI Fig. S9a–d). The obtained parameters are consistent with other reported experimental[29,45] and computational[48] values. Although cell voltage calculations are more challenging, the simulated values are also consistent with the values and trends from experiment, providing additional validity to the simulations. To understand the factors influencing the Mn-rich materials' behaviour, more information on the underlying defect and transport properties is needed on the atomic scale.
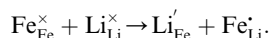
The formation energy of defects in phospho-olivine materials is known to affect their Li$^+$ diffusion properties.[54–56] Here, the formation of point defects (vacancies and antisite pair defects) in LiMn$_x$Fe$_{1-x}$PO$_4$ ($x = 0$, 0.6, 0.7, 0.8, 1) and the energy barrier to lithium-ion diffusion were investigated. Previous modelling[48–50] and experimental[57–59] studies have shown that olivine phosphates suffer from the formation of channel-blocking anti-site defects involving Li/Fe or Li/Mn cation exchange, where a transition metal ion replaces a lithium ion in

Table 1 Calculated and experimental structural parameters and average cell voltages for $LiMn_xFe_{1-x}PO_4$ ($x = 0$, 1 experimental values are from ref. 52 and 53, while $x = 0.6$, 0.7, and 0.8 experimental values from our XRD refinements as described in Section 4.2)

Material	LiFePO$_4$		LiMn$_{0.6}$Fe$_{0.4}$PO$_4$		LiMn$_{0.7}$Fe$_{0.3}$PO$_4$		LiMn$_{0.8}$Fe$_{0.2}$PO$_4$		LiMnPO$_4$	
Parameter	Calc.	Exp.[52]	Calc.	Exp.	Calc.	Exp.	Calc.	Exp.	Calc.	Exp.[53]
a/Å	10.46	10.34	10.55	10.39	10.53	10.38	10.56	10.40	10.59	10.43
b/Å	6.08	6.01	6.14	6.06	6.13	6.05	6.15	6.07	6.17	6.09
c/Å	4.74	4.70	4.77	4.72	4.77	4.71	4.78	4.73	4.79	4.74
Cell voltage/V	3.41	3.45	3.60	3.82	3.52	3.75	3.72	3.88	3.86	4.10

the diffusion channel. This can be described according to the following equation in the case of Fe:

$$Fe^{\times}_{Fe} + Li^{\times}_{Li} \rightarrow Li^{'}_{Fe} + Fe^{\bullet}_{Li}.$$

As the point defects that form are charged, it is energetically favourable for the two anti-site defects to cluster together, forming a defect pair.[48–50] The calculated formation energies for these defect pairs are shown in Fig. 7a. These results indicate that the defects have formation energies of similar magnitude, with almost identical values for the end members LFP and LMP. However, the defect formation energies in the intermediate compositions do not vary linearly between those of the end members. Instead, a clear decrease is found on mixing, with the lowest defect energy for the $x = 0.8$ system. This suggests that Mn/Fe mixing in the lattice makes antisite pair defect formation more favourable so that at equilibrium, higher defect concentrations may be present in the material. The concentration of such anti-site disorder would also be temperature dependent and hence sensitive to experimental synthesis conditions. It is known that antisite defects can block the one-dimensional Li$^+$ diffusion channel, so lower defect formation energies may lead to lower rate capability and higher overpotentials.

Electrodes must have low energy barriers to lithium-ion diffusion to operate well at high rates. However, obtaining insights into ion mobility and pathways for complex mixed-metal polyhedral structures is far from straightforward. Simulation methods can enhance our understanding of the ion diffusion pathway by evaluating the migration energies for various possible mechanisms at the atomic level. Previous studies have shown that Li$^+$ diffusion occurs along the [010] direction,[49,50,60] which has the shortest distance between adjacent lithium sites (3.01 Å).

Calculations were performed to investigate the effect of Mn substitution on Li$^+$ diffusion in the lithiated and delithiated structures. Fig. 7b and c show the simulated diffusion pathway and energy barriers of LMFP and the end members LFP and LMP. The migration barriers obtained are similar for all lithiated compositions, with mixing only slightly increasing the barrier, indicating that any differences in rate capability observed experimentally are not caused by hindered Li$^+$ migration. Higher Li$^+$ migration barriers are found for the lithiated *versus* delithiated structures, suggesting slower kinetics on charge and asymmetric behaviour during cycling.

Although there are no experimental Li$^+$ conductivity data for the Mn-rich compositions for direct comparison, our calculated

migration energies are consistent with measured values for LFP.[3,61] As found in previous investigations, the Li$^+$ diffusion trajectory is a curved, one-dimensional pathway parallel to the b-axis. Similar curved Li$^+$ migration pathways were first predicted from atomistic simulations of LFP which were later confirmed experimentally.[49,50,58,59,62]

The bandgap of electrode materials is known to be linked to electronic conductivity and overpotentials during cell operation, with smaller bandgaps facilitating electronic conduction. From our DFT analysis of the electronic structure changes (density of states shown in Fig. S10), the bandgap of the
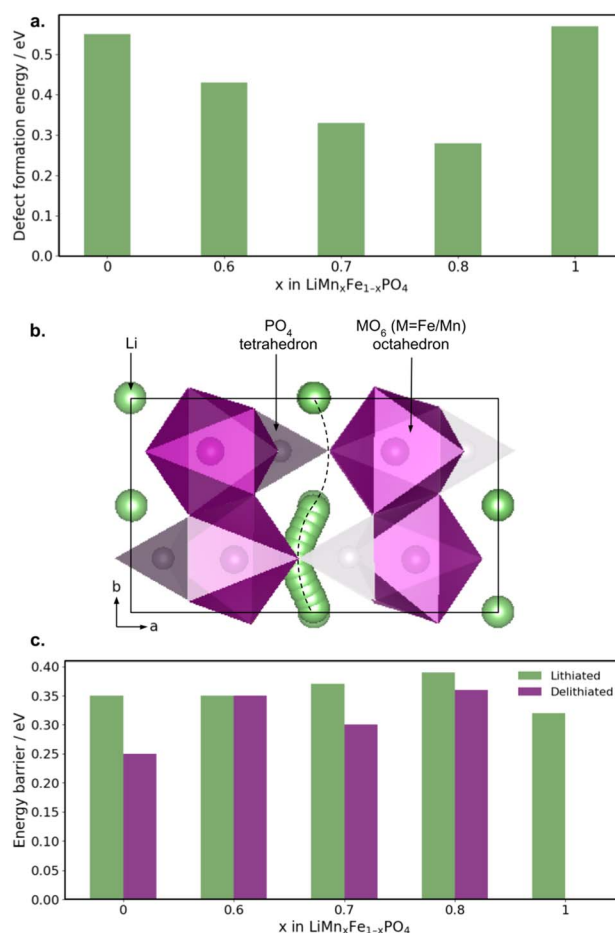

Fig. 7 (a) Lowest defect formation energies calculated for TM-Li$^+$ antisite pair defects for LFP, LMP and Mn-rich LMFP, (b) Li$^+$ diffusion pathway in LiMn$_{0.8}$Fe$_{0.2}$PO$_4$, and (c) energy barriers to Li$^+$ diffusion in LiMn$_x$Fe$_{1-x}$PO$_4$ and Mn$_x$Fe$_{1-x}$PO$_4$ structures.

lithiated structures ranged from 3.43 eV (LMP) to 3.84 eV (LFP), decreasing with higher Mn content; these values are in good agreement with experimental band gaps of 3.8 to 4.0 eV for LFP[63] suggesting sluggish electronic transport behaviour, as observed. The decrease in band gap with higher Mn content indicates that Mn substitution in LMFP can improve the electronic conductivity.

As reported previously,[64] the bandgap of the delithiated phase is lower than that of the lithiated one. From our analysis of the fully delithiated structures, the band gap decreases to 0.55 eV for $Mn_{0.7}Fe_{0.3}PO_4$, with similar values for the mixed Mn/Fe compounds but jumping up to 2.23 eV for $FePO_4$. These asymmetric properties between LMFP and MFP may contribute to the much higher electrode polarisation observed on charge than on discharge when cycling at fast rates. Smaller bandgaps at high charge states may favour electrode homogeneity and a solid solution mechanism during discharge compared to charge, promoting lower overpotentials; this is consistent with the good rate capability on discharge observed in the electrochemical measurements. A future investigation of ion diffusivity through electrochemical impedance spectroscopy is warranted to further elucidate the effect of Fe/Mn mixing on ion conduction in LMFP.

The *ab initio* modelling results suggest that antisite defect formation, though known to be one of the factors that may hinder Li^+ mobility in LMFP, is not the dominant factor affecting ion transport in this Mn-rich system. Fe/Mn mixing reduces the formation energy of antisite defects (Fig. 7), but the 60 and 70% Mn compositions demonstrate similar electrochemical performance while 80% Mn exhibits superior rate capability. This indicates that a competing mechanism must have a larger impact on Li^+ mobility in this system. This could be, for example, due to the increased electronic conductivity, which may be coupled to ionic transport.

3. Conclusions

A systematic multi-technique investigation was carried out on Mn-rich $LiMn_xFe_{1-x}PO_4$ ($x = 0.6, 0.7, 0.8$) cathode materials for high-voltage lithium-ion battery applications. Electrochemical measurements revealed that while compositions with $x > 0.75$ were originally thought to be commercially unviable due to the structural instability of the delithiated Mn-rich phases, these results demonstrate that the operating voltage and rate capability improve with higher Mn concentration up to $x = 0.8$. *Operando* XRD revealed a mixed intercalation mechanism, with a solid solution process at low charge states and two-phase behaviour at high charge states. *Ab initio* simulations show that Li^+ diffusion occurs along *b*-axis one-dimensional channels following a curved trajectory (as in LMP) but may be more susceptible to blocking by Li/Fe and Li/Mn anti-site defect formation. Band gap analysis indicates that Mn substitution of Fe in Mn-rich LMFP can improve the electronic conductivity, as well as suggesting asymmetric electronic behaviour between lithiated (LMFP) and delithiated (MFP) states. Electrochemical measurements demonstrated major differences in electrode polarisation between charge and discharge. These greater

kinetic limitations on charge suggest that a constant voltage hold is required to recover capacity after charging at high rates. This is an essential consideration when designing fast charging protocols for commercial applications and can influence EV performance indicators such as driving range. Overall, considerable asymmetry was observed for Mn-rich LMFP materials between charge and discharge characteristics in terms of electrochemistry, electronic structure and intercalation mechanism.

4. Methods

4.1 Electrode preparation and electrochemical measurements

Battery-grade active material powders for $LiMn_{0.6}Fe_{0.4}PO_4$, $LiMn_{0.7}Fe_{0.3}PO_4$, and $LiMn_{0.8}Fe_{0.2}PO_4$ were provided by SAFT (Bordeaux, France). The synthesis and processing details belong to the active material suppliers, but no significant changes in synthesis parameters were reported for the three materials. The microstructure of the $LiMn_{0.6}Fe_{0.4}PO_4$, $LiMn_{0.7}Fe_{0.3}PO_4$, and $LiMn_{0.8}Fe_{0.2}PO_4$ powders consisted of ovoid sub-micron ($\sim$70 nm) particles (SEM conducted using a QUANTA FEI 200 FEG-ESEM microscope, see SI Fig. S11). The $x = 0.7$ and 0.8 compositions contained agglomerates of the primary particles of diameters up to $\sim$5 μm.

Electrode slurries were prepared by dispersing the active material in 1-methyl-2-pyrrolidone (NMP) with polyvinylidene fluoride (PVDF), binder and carbon additive, forming a slurry composed of 92 wt% active material, 4 wt% conductive agent and 4 wt% PVDF binder in NMP. The slurries were homogenised by several cycles in a planetary mixer (THINKY ARE-250) with mixing balls, after which they were coated onto carbon-coated aluminium foil current collector sheets (0.015 mm thick) using a casting knife and automatic film applicator, then dried at 80 °C. The capacity loading was adjusted to be around 1.5 mAh cm^{-2}; this was calculated considering a theoretical capacity of 170 mAh g^{-1}. The electrodes were calendared to a porosity of around 40% and a thickness of about 0.105 mm.

Electrodes were cut to disks (diameter = 14 mm) and dried at 120 °C under vacuum for at least two hours prior to cell assembly. CR2032-type coin cells were assembled in an argon-filled glovebox ($H_2O \leq 0.5$ ppm, $O_2 \leq 2$ ppm) using a glass fibre separator (Whatman, GE Healthcare, 420 μm thick) and 16 mm diameter battery-grade lithium disk counter electrodes. Approximately 95 μl of a commercial 1 : 1 EC/DMC mixture with 1 M dissolved $LiPF_6$ was used as electrolyte (Solvionic, France). Electrochemical performance was tested using either a VMP-3 potentiostat–galvanostat or a GMP-2 potentiostat–galvanostat (BioLogic, France) in constant current mode with voltage cutoffs of 2.5 to 4.3 V *vs.* Li^+/Li at room temperature (around 20 °C), with charge/discharge rates ranging from C/10 to 3C. The cutoff voltage was held for half an hour before cycling resumed.

Potentiostatic intermittent titration technique (PITT) measurements were carried out at room temperature on each composition to study the phase transitions occurring. CR2032 coin cells, prepared as above, were cycled once at C/10, after which potential was increased in a stepwise manner from 2.5 V

to 4.3 V with a constant step amplitude of $\Delta V = 5$ mV. After each step, the system was allowed to relax until the reduction/oxidation current dropped below a value equivalent to a galvanostatic rate of C/100, calculated based on the theoretical capacity for the material (170 mAh g^{-1}) and the active mass present in that electrode. Integration of the current for each potential level gives incremental capacity. Diffusion behaviour was also investigated using galvanostatic intermittent titration technique (GITT).[45] The cells were cycled once at C/10 between 2.5 and 4.3 V *vs.* Li$^+$/Li, including 1 hour long constant voltage holds at the upper and lower voltage limits, after which they were subjected to 10-minute constant-current pulses at currents equivalent to C-rates of C/10 (calculated from 170 mAh g^{-1}), each followed by 2 hours of rest, until cutoff voltage was reached.

4.2 *Operando* diffraction and spectroscopy

Combined *operando* X-ray diffraction and X-ray absorption near edge spectroscopy experiments were conducted at ALBA Synchrotron (Cerdanyola del Vallès, Spain) at the NOTOS beamline with a wavelength of 0.952729 Å (13 keV). XANES spectra were collected at the Mn (6359 eV) and Fe (7112 eV) K-edges. A Si (111) double crystal monochromator was used with a silicon mirror at 2.2 mrad to perform harmonic rejection. The XANES spectra were collected in transmission mode using ionisation chambers filled with inert gases to absorb about 15% of the photons in the chamber.

Modified 2032-type coin cells with 75 μm thick Kapton windows were assembled in an argon glovebox. The cells contained a 14 mm diameter LMFP electrode, a 16 mm diameter glass fibre separator (Whatman, GE Healthcare, 420 μm thick) and 16 mm diameter commercial 0.45 mm thick commercial, battery-grade Li disks (MTI Corporation, USA). The cells were measured sequentially with a constant time interval between consecutive measurements while the electrochemical testing protocol proceeded. A BioLogic VSP potentiostat was used in galvanostatic mode with a potential limitation (GCPL); the cycling rate was set at C/10 based on the obtainable capacity of the tested material (∼150 mAh g^{-1}) from previous electrochemical tests. This rate was chosen to obtain acceptable time resolution within the limited amount of time available. To decouple reactivity inhibition due to X-ray beam effects from the electrochemistry,[65] measurements were taken at two different spots labelled A and B. At spot A, only XRD was performed, while XRD and XANES were taken at spot B, therefore delivering a significantly higher radiation dose. Comparison between spots A and B at the equivalent measurement points then serves as an indication of the severity of the beam effects on the samples. XRD patterns were first treated *via* the LeBail refinement (profile matching) method to obtain lattice parameters, after which they underwent Rietveld refinement using FullProfAPP.[66] The patterns were fit with two phases (LMFP73 and MFP73) with the orthorhombic space group *Pnma* with slight variations in the lattice parameters allowed. The *operando* XAS data was process with FDA (Fast Data Analyzer) software.[67]

4.3 Computational methods

Density functional theory (DFT) calculations were performed using the VASP plane wave code using projector augmented wave method pseudopotentials.[68] Bulk structural optimisations were conducted with a plane wave cutoff energy of 520 eV and a *k*-point spacing of 0.25/2π for unit cell optimisations. Effective Hubbard *U* values were selected to match the Materials Project database recommendations.[69,70] The unit cells of FePO$_4$, MnPO$_4$, LiFePO$_4$ and LiMnPO$_4$ were relaxed, and average cell voltages against lithium were calculated. For the general delithiation reaction.

$$\text{Li}_x[\text{cathode}] + (x' - x)\text{Li}[\text{anode}] \rightarrow \text{Li}_{x'}[\text{cathode}]$$

where *x* and *x'* are the initial and final degrees of lithiation, respectively, the average potential is

$$V(x) = \frac{-\Delta G}{(x' - x)F},$$

where ΔG is the change in Gibbs free energy on delithiation and *F* is the Faraday constant. The entropic contributions to ΔG are negligible at room temperature, so enthalpy dominates the equation,[71] allowing average deintercalation voltage to be approximated as:

$$V_{\text{average}} = -\frac{E(\text{Li}_x\text{MPO}_4) - E\left(\text{Li}_{x'}\text{MPO}_4\right) - \left(x - x'\right)E(\text{Li}_{\text{bulk}})}{e(x' - x)}$$

where *E*(structure) is a structure's energy per formula unit and *e* is electronic charge. The average voltages calculated using different functionals were compared to experimental values to select the best-performing functional. Geometry optimisations were run for LiFePO$_4$ using a range of DFT functionals (LDA, PBE, PBEsol, PBE + *U*, PBEsol + *U*, R2SCAN and B3LYP). The calculated energies were used to estimate average cell voltage, shown in Table 2. PBE + *U* matched experimental values best,[31] and was therefore used in calculations.

Following this initial benchmarking on the LFP and LMP structures, the DFT calculations were repeated for 1 × 5 × 2 supercells with varying Mn to Fe ratios (*x* = 0.6, 0.7, 0.8 and 1) using the same calculation parameters. A value for pure MnPO$_4$ could not be obtained due to the excessive Jahn–Teller distortions caused by the Mn^{3+} ion; this is also why MnPO$_4$ is not a viable electrode candidate.[72] The input Li$_y$Mn$_x$Fe$_{1-x}$PO$_4$ (*y* = 0 or 1, *x* = 0.6, 0.7, 0.8) structures were generated by taking a weighted average of the unit cell parameters from the corresponding Li$_y$MnPO$_4$ and Li$_y$FePO$_4$ structures and using the icet

Table 2 Calculated and experimental[1] average cell voltages *vs.* Li$^+$/Li for LiFePO$_4$ using various DFT functionals. *U* = 5.3 eV for iron

Exp.[1]	PBE + *U*	B3LYP	LDA	PBEsol	PBE	R2SCAN
3.45	3.45	3.36	3.00	2.85	2.78	2.41

python package[73] with 3×10^5 steps to generate special quasirandom structures with the desired Mn : Fe ratio.[74,75] DFT calculations were performed to study the defect formation energies of antisite pair defects in LMFP with various compositions. The PBE + U_{eff} functional was used with a plane wave cutoff energy of 520 eV and a maximal k-point spacing of $0.25/2\pi$ (0.04 per Å). The smallest possible supercell size, $1 \times 1 \times 5$, was used to reduce computational cost while achieving the desired TM ratios of 60, 70, and 80% Mn. These underwent geometry optimisations, after which defects were manually generated. For the antisite disorder calculations, four antisite supercells were generated for each composition, creating cation exchange defect pairs with both iron and manganese. Of these calculations, the lowest-energy defect pair was then selected, as this would be the more energetically favourable defect.

Nudged elastic band (NEB) calculations were conducted to analyse the energetics of lithium-ion diffusion within these materials using the VTST library and its corresponding force optimisers.[76] $1 \times 2 \times 5$ supercells of the desired LMFP composition were constructed and allowed to relax with the geometry optimisation protocol described previously, after structures with a single Li$^+$ vacancy each were optimised. For Li$^+$ diffusion in the delithiated structures, the reverse was done, relaxing the delithiated structure after adding a single lithium-ion. Optimised structures with neighbouring vacancies/ions along the channels parallel to the crystallographic b-axis were used as the NEB endpoints, and the climbing image (CI) algorithm was used to create 9 intermediate images between the two minima by linear interpolation between the endpoints and a spring constant of 5 eV Å^{-1} between consecutive images. The minimum energy diffusion path (MEP) was calculated. The limited-memory Broyden–Fletcher–Goldfarb–Shanno (LBFGS) algorithm was used to optimise the MEP in a fixed supercell until a force below 10^{-2} eV Å^{-1} was obtained.

Author contributions

B. R.: data curation, formal analysis, investigation, methodology, validation, visualisation, writing – original draft, review & editing. F.-C. M.: methodology, software, supervision, writing – review & editing. D. C.: methodology, supervision. V. F. and A. P. B.: methodology, data formal analysis, visualisation, writing. B. C., C. T., P. B.; supervision, resources, writing – review & editing. M. S. I.: conceptualisation, funding acquisition, resources, supervision, writing – review & editing. M. R. P.: conceptualisation, funding acquisition, resources, supervision, writing – review & editing.

Conflicts of interest

There are no conflicts to declare.

Data availability

Data supporting this article has been included in the main manuscript and supplementary information (SI). Additional data will be made available from the corresponding author upon reasonable request. Supplementary information: electrochemical data, X-ray *operando* data, DFT simulated lattice parameters and partial densities of states, and SEM micrographs of the electrodes. See DOI: https://doi.org/10.1039/d5ta10330d.

Acknowledgements

Notes and references

1 A. K. Padhi, K. S. Nanjundaswamy and J. B. Goodenough, *J. Electrochem. Soc.*, 1997, **144**, 1188–1194.

2 H. Liu, F. Nozaki, J. Hwang and K. Matsumoto, *J. Power Sources*, 2025, **620**, 1–20.

3 L.-X. Yuan, Z.-H. Wang, W.-X. Zhang, X.-L. Hu, J.-T. Chen, Y.-H. Huang and J. B. Goodenough, *Energy Environ. Sci.*, 2010, **4**, 269–284.

4 G. Bree, J. Zhao, V. Majherova, D. Proprentner, G. J. P. Fajardo and L. F. J. Piper, *Energy Fuels*, 2025, **39**, 3683–3689.

5 G. Zhang, D. Kong, S. Zhou, J. Liu, Y. Wang, J. Miao, L. Jia, Q. Dong, H. Liu, H. Shao, Y. Shen and L. Chen, *Batter. Supercaps*, 2025, 1–6.

6 X. Zhang, M. Hou, A. G. Tamirate, H. Zhu, C. Wang and Y. Xia, *J. Power Sources*, 2020, **448**, 6992–6996.

7 C. Delacourt, L. Laffont, R. Bouchet, C. Wurm, J.-B. Leriche, M. Morcrette, J.-M. Tarascon and C. Masquelier, *J. Electrochem. Soc.*, 2005, **152**, A913–A921.

8 L. Yang, W. Deng, W. Xu, Y. Tian, A. Wang, B. Wang, G. Zou, H. Hou, W. Deng and X. Ji, *J. Mater. Chem. A*, 2021, **9**, 14214–14232.

9 Y. Deng, C. Yang, K. Zou, X. Qin, Z. Zhao and G. Chen, *Energy Mater.*, 2017, **7**, 1–29.

10 J. M. Gonçalves, S. Mubarac, G. T. M. Silva, B. Freitas, B. G. Aguiar Neto and H. Zanin, *J. Mater. Chem. A*, 2025, 1–31.

11 Q. Pan, Z. Qin, C. Lei, J. Peng, Z. He, Y. Li, G. Huo and Y. Cheng, *J. Power Sources*, 2026, **662**, 1–10.

12 M. Parvin, S. Bhowmik, M. Bhar and S. K. Marthaz, *J. Electrochem. Soc.*, 2025, **172**, 1–9.

13 S. Y. Jeong, S. Lee, H. Lee, K.-M. Roh, C.-W. Lee, I. Jeong and M. S. Chae, *J. Power Sources*, 2025, **626**, 1–7.

14 J. Liu, Y. Wu, B. Zhang, X. Xiao, Q. Hu, Q. Han, L. Wang, F. Bei and X. He, *Small*, 2024, **20**, 1–9.

15 E. Xu, T. Wang, J. Chen, J. Hu, H. Xia, H. Wu, W. Cai, Q. Zhang, Y. Zhang and K. Wu, *Adv. Energy Mater.*, 2024, **15**, 1–16.

16 J. Ding, Z. Su and H. Tian, *Ceram. Int.*, 2016, **42**, 12435–12440.

17 H. Du, Y. Kang, C. Li, Y. Zhao, J. Wozny, T. Li, Y. Tian, J. Lu, L. Wang, F. Kang, N. Tavajohi and B. Li, *Battery Energy*, 2023, **2**, 1–9.

18 H. Dou, J. Huang, F. Zhang, F. Zong, X. Zhou, D. Zhao, N. Zhang, X. Cui, S. Li and P. Wang, *J. Power Sources*, 2025, **656**, 1–10.

19 P. Wang, Y. Fang, E. Zhang, L. Chen, H. Yu, Q. Cheng and H. Jiang, *J. Mater. Chem. A*, 2025, **13**, 22155–22162.

20 S. Li, J. Wang, Y. Liu, Z. Liu, H. Zhang, L. Wang and X. He, *Adv. Funct. Mater.*, 2025, **35**, 1–10.

21 M. Yao, Y.-T. Wang, J.-A. Chen, H. Dong, M. Li, X. Zhang, C. Wang, G. Huang and S. Xu, *ACS Appl. Mater. Interfaces*, 2024, **16**, 66077–66088.

22 K. Leslie, J. Harlow, D. Rathore, K. Tuul and M. Metzger, *J. Electrochem. Soc.*, 2024, **171**, 1–11.

23 A. Aishova, M. Johnson, L. Zhang, N. Zaker, B. S. Amirkhiz, J. R. Dahn and M. Metzger, *Chem. Mater.*, 2025, **37**, 7635–7647.

24 C. Chak, V. Shipitsyn and L. Ma, *J. Electrochem. Soc.*, 2025, **172**, 1–6.

25 G. Bree, V. Majherova, E. Fiamegkou, S. Moharana and L. F. J. Piper, *J. Electrochem. Soc.*, 2025, **172**, 1–8.

26 Y. Wang, C.-Y. Wu, H. Yanga and J.-G. Duh, *J. Mater. Chem. A*, 2018, **6**, 10395–10403.

27 J. Li, M. Xiang, Y. Wang, J. Wu, H. Zhao and H. Liu, *J. Mater. Chem. A*, 2017, **5**, 7952–7960.

28 S. K. Martha, J. Grinblat, O. Haik, E. Zinigrad, T. Drezen, J. H. Miners, I. Exnar, A. Kay, B. Markovsky and D. Aurbach, *Angew. Chem.*, 2009, **48**, 8559–8563.

29 A. Yamada, Y. Kudo and K. Liu, *J. Electrochem. Soc.*, 2001, **148**, A747–A754.

30 O. A. Drozhzhin, V. D. Sumanov, O. M. Karakulina, A. M. Abakumov, J. Hadermann, A. N. Baranov, K. J. Stevenson and E. V. Antipov, *Electrochim. Acta*, 2016, **191**, 149–157.

31 V. Aravindan, J. Gnanaraj, Y. Lee and S. Madhavi, *J. Mater. Chem. A*, 2013, **1**, 3518–3539.

32 T. A. Wani and G. Suresh, *J. Energy Storage*, 2021, **44**, 1–57.

33 J. Lee, M. Park, B. Anass, J. Park, M. Paik and S. Doo, *Electrochim. Acta*, 2010, **55**, 4162–4169.

34 B. Zhang, X. Wang, H. Li and X. Huang, *J. Power Sources*, 2011, **196**, 6992–6996.

35 W. Ling, S. Fang, W. Zhou, C. Ye, L. Wang, N. Zhou and X. He, *Adv. Energy Mater.*, 2025, **15**, 1–30.

36 M. Zhao, Y. Zhou, Y. Chen, X. Liang, J. Zeng, K. Bai, X. Xu, H. Wang, X. Jiang and H. He, *Adv. Funct. Mater.*, 2025, 1–14.

37 S. Li, H. Zhang, Y. Liu, L. Wang and X. He, *Adv. Funct. Mater.*, 2024, **34**, 1–27.

38 D. D. Lecce and J. Hasson, *J. Phys. Chem. C*, 2015, **119**, 20855–20863.

39 S. Li, X. Meng, Q. Yi, J. A. Alonso, M. T. Fernández-Díaz, C. Sun and Z. L. Wang, *Nano Energy*, 2018, **52**, 510–516.

40 Q. Hu, L. Wang, G. Han, J. Liao, J. Liu, J. Yao and X. He, *Nano Energy*, 2024, **123**, 1–9.

41 H. Zheng, L. Chai, X. Song and V. Battaglia, *Electrochim. Acta*, 2012, **62**, 256–262.

42 W. M. Dose, W. Li, I. Temprano, C. A. O'Keefe, B. L. Mehdi, M. F. L. D. Volder and C. P. Grey, *ACS Energy Lett.*, 2022, **7**, 3524–3530.

43 S. Solchenbach, M. Metzger, M. Egawa, H. Beyer and H. A. Gasteiger, *J. Electrochem. Soc.*, 2018, **165**, A3022–A3028.

44 M. Metzger, J. Sicklinger, D. Haering, C. Kavakli, C. Stinner, C. Marino and H. A. Gasteiger, *J. Electrochem. Soc.*, 2015, **162**, A1227–A1235.

45 S. Niu, X. Bing, J. You, L. Sheng, W. Zhou, J. Li, M. Cao, S. Chen, J. Yang, L. Tao, C. Tan and S. Xin, *Acta Mater.*, 2025, **293**, 1–11.

46 A. Losey, J. Rakovan, J. M. Hughes, C. A. Francis and M. D. Dyar, *Can. Mineral.*, 2004, **42**, 1105–1115.

47 P. Zhu, P. R. Slater and E. Kendrick, *Mater. Des.*, 2022, **223**, 1–20.

48 G. R. Gardiner and M. S. Islam, *Chem. Mater.*, 2010, **22**, 1242–1248.

49 C. A. J. Fisher, V. M. H. Prieto and M. S. Islam, *Chem. Mater.*, 2008, **20**, 5727–5938.

50 M. S. Islam, D. J. Driscoll, C. A. J. Fisher and P. R. Slater, *Chem. Mater.*, 2005, **17**, 4889–5224.

51 K. McColl, S. W. Coles, P. Zarabadi-Poor, B. J. Morgan and M. S. Islam, *Nat. Mater.*, 2024, **23**, 826–833.

52 G. Rousse, J. Rodriguez-Carvajal, S. Patoux and C. Masquelier, *Chem. Mater.*, 2003, **15**, 4082–4090.

53 O. García-Moreno, M. Alvarez-Vega, F. García-Alvarado, J. García-Jaca, J. M. Gallardo-Amores, M. L. Sanjuán and U. Amador, *Chem. Mater.*, 2001, **13**, 1570–1576.

54 A. Paolella, S. Turner, G. Bertoni, P. Hovington, R. Flacau, C. Boyer, Z. Feng, M. Colombo, S. Marras, M. Prato, L. Manna, A. Guerfi, G. P. Demopoulos, M. Armand and K. Zaghib, *Nano Lett.*, 2016, **16**, 2692–2697.

55 Y. Xiao, Z. Zhao, Q. Zhang and R. Qiao, *ACS Omega*, 2025, **10**, 1293–1302.

56 J. Chen and J. Graetz, *Appl. Mater. Interfaces*, 2011, **3**, 1380–1384.

57 S.-Y. Chung, S.-Y. Choi, T. Yamamoto and Y. Ikuhara, *Phys. Rev. Lett.*, 2008, **100**, 1–4.

58 J. V. Laveda, B. Johnston, G. W. Paterson, P. J. Baker, M. G. Tucker, H. Y. Playford, K. M. Ø. Jensen, S. J. L. Billinge and S. A. Corr, *J. Mater. Chem. A*, 2018, **6**, 127–137.

59 A. Paolella, G. Bertoni, P. Hovington, Z. Feng, R. Flacau, M. Prato, M. Colombo, S. Marras, L. Manna, S. Turner, G. V. Tendeloo, A. Guerfi, G. P. Demopoulos and K. Zaghib, *Nano Energy*, 2015, **16**, 256–267.

60 L. Wang, F. Zhou, Y. S. Meng and G. Ceder, *Phys. Rev. B: Condens. Matter Mater. Phys.*, 2007, **76**, 1–11.

61 J. Li, W. Yao, S. Martin and D. Vaknin, *Solid State Ionics*, 2008, **179**, 2016–2019.

62 S.-I. Nishimura, G. Kobayashi, K. Ohoyama, Y. Kanno, M. Yashima and A. Yamada, *Nat. Mater.*, 2008, **7**, 707–711.

63 F. Zhou, K. Kang, T. Maxisch, G. Ceder and D. Morgan, *Solid State Commun.*, 2004, **132**, 181–186.

64 D. Kwon and D. Kim, *Adv. Energy Mater.*, 2025, **2501444**, 1–9.

65 A. P. Black, C. Escudero, F. Fauth, M. Fehse, G. Agostini, M. Reynaud, R. G. Houdeville, D. Chatzogiannakis, J. Orive, A. Ramo-Irurre, M. Casas-Cabanas and M. R. Palacín, *Chem. Mater.*, 2024, **36**, 5239–5858.

66 O. Arcelus, J. Rodriguez-Carvajal, N. A. Katcho, M. Reynaud, A. P. Black, D. Chatzogiannakis, C. Frontera, J. Serrano-Sevillano, M. Ismail, J. Carrasco, F. Fauth, M. R. Palacin and M. Casas-Cabanas, *J. Appl. Crystallogr.*, 2024, **57**, 1676–1690.

67 C. Marini and S. Toutounchiavval, *J. Phys.: Conf. Ser.*, 2025, **3010**, 1–6.

68 G. Kresse and J. Furthmiiller, *Comput. Mater. Sci.*, 1996, **6**, 15–50.

69 F. Zhou, M. Cococcioni, C. A. Marianetti, D. Morgan and G. Ceder, *Phys. Rev. B: Condens. Matter Mater. Phys.*, 2004, **70**, 1–8.

70 M. Wang and A. Navrotsky, *Solid State Ionics*, 2004, **166**, 167–173.

71 M. S. Islam and C. A. J. Fisher, *Chem. Soc. Rev.*, 2014, **43**, 185–204.

72 G.-X. Zhang, A. M. Reilly, A. Tkatchenko and M. Scheffler, *New J. Phys.*, 2018, **20**, 1–19.

73 M. Ångqvist, W. A. Muñoz, J. M. Rahm, E. Fransson, C. Durniak, P. Rozyczko, T. H. Rod and P. Erhart, *Adv. Theory Simul.*, 2019, **2**, 1–10.

74 A. Zunger, S.-H. Wei, L. G. Ferreira and J. E. Bernard, *Phys. Rev. Lett.*, 1990, **65**, 353–356.

75 A. V. D. Walle, P. Tiwary, M. D. Jong, D. L. Olmsted, M. Asta, A. Dick, D. Shin, Y. Wang, L.-Q. Chen and Z.-K. Liu, *CALPHAD: Comput. Coupling Phase Diagrams Thermochem.*, 2013, **42**, 13–18.

76 G. Henkelman, B. P. Uberuaga and H. Jónsson, *J. Chem. Phys.*, 2000, **113**, 9901–9904.